Weyl nodal-ring semimetallic behavior and topological superconductivity in crystalline forms of Su-Schrieffer-Heeger chains

Peter Rosenberg [1,2] and Efstratios Manousakis [2,3]

[1]*Département de Physique & Institut Quantique, Université de Sherbrooke, Québec, Canada J1K 2R1*
[2]*National High Magnetic Field Laboratory and Department of Physics, Florida State University, Tallahassee, Florida 32306, USA*
[3]*Department of Physics, National and Kapodistrian University of Athens, Panepistimioupolis, Zografos, 157 84 Athens, Greece*

We consider a three-dimensional model of coupled Su-Schrieffer-Heeger (SSH) chains. The analytically soluble model discussed here reliably reproduces the features of the band structure of crystalline polyacetylene as obtained from density-functional theory. We show that when a certain interchain coupling is sufficiently increased, the system develops a ring of Weyl nodes. We argue that such an increase could be achieved experimentally by intercalation or extreme pressure. With the addition of a simple intraorbital pairing term we find that the system supports an exotic superconducting state with drumhead surface states and annular Majorana states localized on the surface. In addition to suggesting a real material realization of a nodal ring semimetal and possibly topological superconductivity, our results provide a different perspective on the SSH model, demonstrating that a simple extension of this broadly impacting model can once again provide fundamental insights on the topological behavior of condensed matter systems.

I. INTRODUCTION

Since its introduction over four decades ago, the Su-Schrieffer-Heeger (SSH) model [1] has served as a beautiful and rather simply understood example of emergent quasiparticles, qualitatively different from those in the noninteracting system. The model was inspired by quasi-one-dimensional materials such as polyacetylene, and despite its apparent simplicity, has proven to be a tremendously rich description that captures a variety of fascinating phenomena, including solitons, topological transitions, edge states, and charge fractionalization [2,3]. The SSH model also provided one of the earliest examples of a nontrivial one-dimensional Berry phase, known as the Zak phase [4], in a condensed matter system.

These early notions of topology, first explored within the context of the SSH model and in the quantum Hall effect, have become a central focus of modern condensed matter physics. This renewed interest in the role of topology in condensed matter systems was primarily motivated by the discovery of topological insulators [5]. More recently a new class of topological materials has been discovered, the Dirac and Weyl semimetals [6–12]. These materials are defined by the presence of a set of topologically protected band touching points, which lead to unique transport properties. The set of proposed topological semimetals has since been expanded to include systems with lines or rings of degeneracies in their band structures, which have been termed nodal-line or nodal-ring semimetals [13–16]. Several examples of these systems have already been proposed or reported in real materials [17–19]. These novel materials hold the promise of many impactful applications, making a reliable description of their exotic behaviors a priority of condensed matter physics.

In this paper we provide a different perspective on the well-studied SSH model, illustrating that this relatively simple description, which yielded some of the earliest insights into the topology of condensed matter systems, can be adapted straightforwardly to describe the physics of topological nodal semimetals. We present a three-dimensional (3D) analytically soluble model, inspired by the structure of crystalline polyacetylene, consisting of coupled SSH chains. We show that with an appropriate choice of the hopping parameters it reliably reproduces the features of the band structure of crystalline polyacetylene, as obtained from density-functional theory (DFT). In addition, we demonstrate that the band structure of this model, when a diagonal hopping parameter is increased, contains a Weyl nodal ring. It is conceivable that this parameter regime could be experimentally accessed by application of extreme pressure on crystalline polyacetylene. We also find that, with the addition of simple pairing interactions, the model supports a topological superconducting phase characterized by the presence of surface Majorana fermions. While our model could be realized experimentally in the context of conjugated polymers, it is just as relevant to the case of cold atoms, where there has been remarkable progress in the realization of topological lattice models [20,21], including Weyl semimetals [22] and nodal-ring semimetals [23].

The observation of superconductivity in topological systems has brought considerable attention to the problem of the interplay of strong correlations and pairing with topology, including in the context of Dirac and Weyl semimetals [24–30], as well as nodal-line semimetals [31–33], which may support exotic superconducting phases. Many models are known to support topological superconductivity, typically characterized by the presence of Majorana surface or edge states. Most
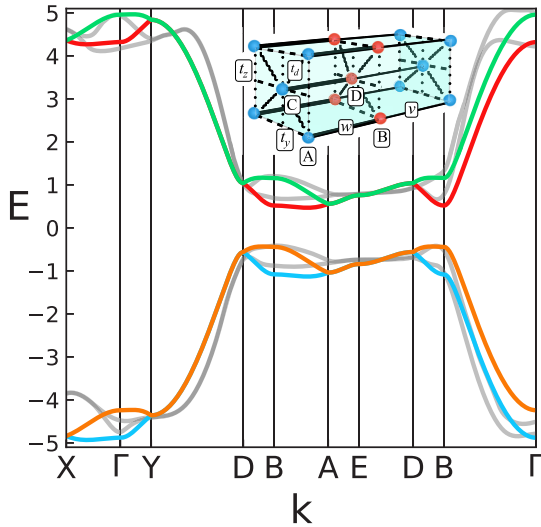
FIG. 1. Tight-binding vs DFT band structure. We show the band structure obtained from our lattice model, compared to density-functional theory results using the experimentally measured structural parameters [35]. We include an overall shift to the DFT results to restore particle-hole symmetry about $E = 0$. The inset shows the unit cell with relevant hopping elements

FIG. 2. (a) Unit cell of modified lattice TB model. (b) Nodal points in the k_x-k_y plane at $k_z = \pi/4$. (c), (d) Band structure in the k_y-k_z plane at different values of k_x. (c) $k_x = \pi/4$. (d) $k_x = 0$. The nodal line at $k_x = 0$, which bounds the drumhead surface state (light red), is highlighted in red. The model parameters are $v = 2.7$, $w = 1.9$, $t_d' = 1.0$, $t_d = t_y = t_z = 0$, and we take $a_x = a_y = a_z = 1$.

theoretical descriptions of these exotic superconducting states assume the presence of p-wave or higher angular momentum pairing terms. However, it was recently noted that topological superconducting states can emerge from conventional s-wave pairing interactions in Weyl systems. In these systems each Weyl node is split by the interaction into a pair of Bogoliubov-Weyl [24,26,34] nodes and Majorana states appear at the boundaries. This behavior has also been recently explored in nodal-ring semimetals [33] and does indeed emerge in our model with the addition of an interorbital pairing term.

II. MODEL

We begin with a simplified tight-binding (TB) model of the $P2_1/a$ structure of crystalline *trans*-polyacetylene, as depicted in Fig. 2 of Ref. [35]. Our model keeps all the relevant elements and symmetry aspects of the real structure, but is simple enough to permit an exact solution. This compromise is made in order to project out and provide a clear understanding of the physics of this system. Despite its apparent simplicity, the model shows remarkable agreement with the DFT calculation.

In the inset of Fig. 1 we present the unit cell and hopping elements for our model, which provides a qualitative description of the important features of the band structure of the $P2_1/a$ structure of crystalline *trans*-polyacetylene. The dimerized SSH chains are along the x axis. The red and blue spheres represent carbon atoms whose color corresponds to their relative position along the dimerized chain (A or B sublattice). The dimerization leads to two different hopping matrix elements, denoted here as w and v, along the chain. These SSH chains run parallel to each other, forming the unit cell depicted in the inset of Fig. 1. Though depicted here as collinear, in polyacetylene the carbon atoms do not lie along a straight line, rather forming bonds of $120°$ to facilitate the sp^2 hybridization of the $2s$ and two of the three $2p$ orbitals that form the bonds
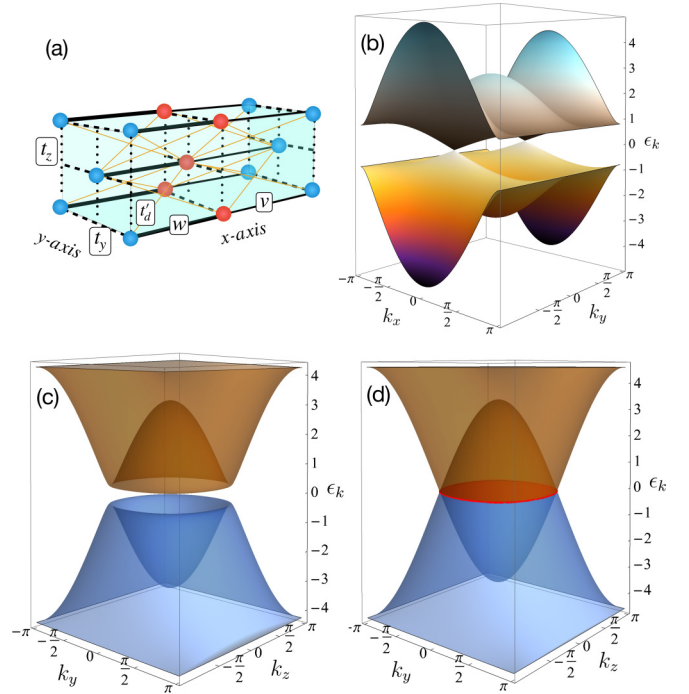
of the carbon atom with its nearest neighboring carbon atom and a hydrogen atom (neglected in the structure depicted in Fig. 1). The hopping of the third $2p$ (call it $2p_z$) electron of the carbon atom forms the bands near the Fermi level. While the physical presence of the hydrogen atoms along each chain and their relative orientation is important in determining the effective interchain hopping matrix elements, these atoms are also abstracted out of our drawing for simplicity.

In addition to the hoppings w and v, we consider a carbon to carbon interchain hopping matrix element along the y (t_y) and the z (t_z) directions. We also include a hopping matrix element along the diagonal (0,1,1) direction (t_d). The most general version of the model includes an additional hopping along the (1,1,1) direction (t_d') [depicted in Fig. 2(a)], but we first consider the limit $t_d' \to 0$, corresponding to the unit cell shown in Fig. 1. The unit cell is doubled along the x direction because of the dimerization along that direction; however, the interchain hopping matrix elements are independent of whether the hopping is between carbon atoms on the A sublattice or the B sublattice.

The TB Hamiltonian of the structure is given in k space as $\hat{H}_0 = \sum_{\mathbf{k}} c_{\mathbf{k}}^{\dagger} \mathcal{H}_0(\mathbf{k}) c_{\mathbf{k}}$, with

$$\mathcal{H}_0(\mathbf{k}) = \begin{pmatrix} e(\mathbf{k}) & S & V & V' \\ S^* & e(\mathbf{k}) & V' & V \\ V & V' & e(\mathbf{k}) & S \\ V' & V & S^* & e(\mathbf{k}) \end{pmatrix}, \quad (1)$$
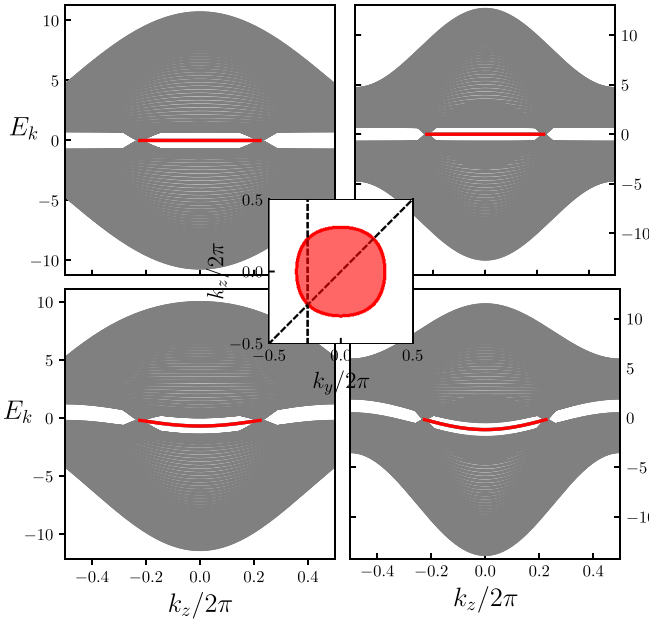
FIG. 3. Surface states vs k_z for a slab open along x. The surface state is highlighted in red. The top two panels show the edge spectrum with $t_y = t_z = 0$, and the bottom panels show the surface spectrum for $t_y = t_z = 0.3$ (the remaining parameters are the same as in Fig. 2). The left column is along the cut $k_y/2\pi = -0.228$, and the right column is along $k_y = k_z$. Inset: Nodal ring in the k_y-k_z plane and drumhead state in the shaded red region. The dashed lines correspond to the cuts used for the two columns.

where $c_{\mathbf{k}}^{\dagger} = (c_{\mathbf{k}}^{\dagger(A)} \quad c_{\mathbf{k}}^{\dagger(B)} \quad c_{\mathbf{k}}^{\dagger(C)} \quad c_{\mathbf{k}}^{\dagger(D)})$ is the set of creation operators for electrons in the $2p_z$ state on the A, B, C, and D atoms (see Fig. 1 for labels), and

$$e(\mathbf{k}) = -2t_y \cos(k_y a_y) - 2t_z \cos(k_z a_z), \quad (2)$$

$$S = X + iY, \quad (3)$$

$$X = (v + w) \cos(k_x a_x/2), \quad (4)$$

$$Y = (v - w) \sin(k_x a_x/2), \quad (5)$$

$$V = -4t_d \cos(k_y a_y/2) \cos(k_z a_z/2), \quad (6)$$

$$V' = -8t_d' \cos(k_x a_x/2) \cos(k_y a_y/2) \cos(k_z a_z/2). \quad (7)$$

All hopping parameters are in units of eV.

We first consider the case of $t_d' = 0$. Our model can be diagonalized exactly and has the following set of bands:

$$E_1^{\pm}(\mathbf{k}) = -2t_y \cos(k_y a_y) - 2t_z \cos(k_z a_z)$$
$$\pm \sqrt{X^2 + Y^2 + V^2 + 2|V|\sqrt{X^2 + Y^2}},$$

$$E_2^{\pm}(\mathbf{k}) = -2t_y \cos(k_y a_y) - 2t_z \cos(k_z a_z)$$
$$\pm \sqrt{X^2 + Y^2 + V^2 - 2|V|\sqrt{X^2 + Y^2}}. \quad (8)$$

In Fig. 1 we compare the bands from our TB model to the band structure obtained via DFT using the experimentally determined structural parameters [35]. We observe that the

features of the DFT band structure (gray curves in the figure) are well reproduced.

III. NODAL-RING SEMIMETAL AND DRUMHEAD STATES

We now consider a related, analytically soluble model, by taking the limit of $t_d \to 0$ while $t_d' \neq 0$, and illustrate that this simple modification of the previous model can realize a 3D Weyl nodal-ring semimetal. We note that for the structure depicted in Fig. 2 (i.e., $P2_1/a$) this requires the second closest neighbor hopping (diagonal, blue to red) to be dominant over the closest neighbor hopping (diagonal, blue to blue), which may be difficult to achieve experimentally. However, the Hamiltonian corresponding to this case has an identical form to the Hamiltonian for the $P2_1/n$ structure (see Appendix A), with the second closest neighbor hopping t_d' becoming a closest neighbor hopping. This Hamiltonian, with larger interchain-hopping matrix elements, may be realized by the application of extreme pressure, which should make the system more three dimensional, as opposed to the currently experimentally accessible structure that has a quasi-1D nature. The application of high pressure may stabilize one or the other structure, both of which support nodal-ring states. Additionally, while we focus on the limit of $t_d \to 0$ for demonstration, because it permits an analytic solution, we observe that the nodal-ring state exists across a broad parameter regime, including for the case of both finite t_d and t_d', and is also robust with respect to the magnitudes of t_y and t_z (see Fig. 3).

The eigenvalues in this case ($t_d = 0, t_d' \neq 0$) are the following four bands:

$$E_{\pm}^{+}(\mathbf{k}) = e(\mathbf{k}) \pm \lambda_+, \quad (9)$$

$$E_{\pm}^{-}(\mathbf{k}) = e(\mathbf{k}) \pm \lambda_-, \quad (10)$$

$$\lambda_{\pm} = \sqrt{(|X| \pm |V'|)^2 + Y^2}. \quad (11)$$

A ring of Weyl nodes is formed by the $E_{\pm}^{-}$ bands at the set of momenta satisfying the equations, $Y = 0$, $|X| = |V'|$. The solutions to these equations are

$$k_x = 0, \quad \left|\cos\left(\frac{k_z a_z}{2}\right)\right|\left|\cos\left(\frac{k_y a_y}{2}\right)\right| = \frac{v + w}{8t_d'}, \quad (12)$$

which specify a nodal ring, provided $r \equiv (v + w)/(8t_d') \leqslant 1$. We show an example of the nodal ring in Appendix B.

In Figs. 2(c) and 2(d) we illustrate the emergence of the nodal ring in the bulk band structure as the value of k_x approaches zero. For clarity we show only $E_{\pm}^{-}$, and note that the $E_{\pm}^{+}$ bands do not participate in the formation of the nodal ring. When we fix k_z (or k_y) and plot the band structure in the k_x-k_y (or k_x-k_z) plane we observe a pair of Weyl nodes [see Fig. 2(b)], the full set of which, obtained by varying k_y and k_z, forms the nodal line.

When the system is finite in the x direction, a doubly degenerate drumhead surface state bounded by the nodal ring forms [36]. This surface state is depicted in red in Fig. 2(d). The surface spectrum is plotted versus k_z in Fig. 3 for two different choices of the hopping parameter t_y and t_z and for two values of k_y. The drumhead surface state is again highlighted in red. Notice that when t_y and t_z are nonzero, the drumhead state becomes dispersive.
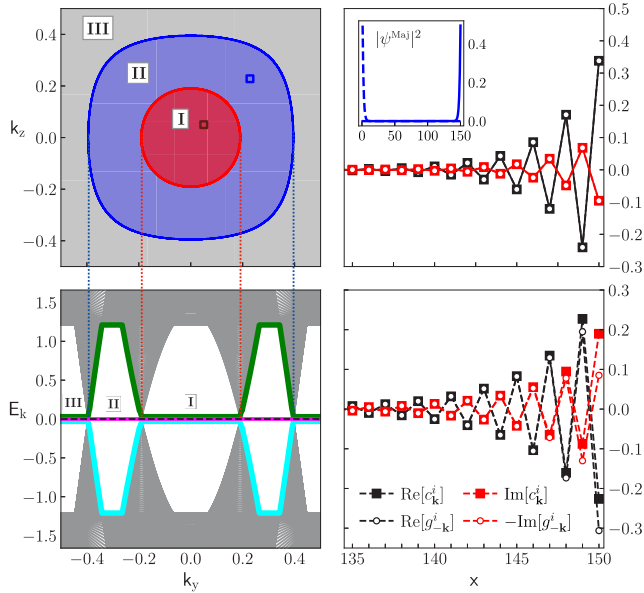
FIG. 4. Nodal rings, surface spectrum, and wave-function amplitudes. Upper left: Projected nodal ring in the k_y-k_z plane, with $\mu = 0.2$, $\Delta = 2.0$ (k_y and k_z are in units of 2π and the remaining parameters are identical to Fig. 2). Region I contains four drumhead states, region II, two annular Majorana surface states, and region III, four annular Majorana surface states. Lower left: Surface spectrum along the k_y axis. The vertical dashed lines are a guide to the eye for the region boundaries. We plot the surface states in color. Upper right: Components of the wave function for a Majorana state at the momentum indicated by the blue box in the upper left panel. The inset shows the square modulus of the wave function for the two Majorana states at this momentum. Lower right: Components of the wave function for a surface state at the momentum indicated by the red box in the upper left panel.

IV. BERRY PHASE

The eigenstates of the $\lambda_-(\mathbf{k})$ eigenvalue, which correspond to the band with Weyl character, are given by the vector $|\psi^-\rangle$ with components $a = (V' - \epsilon S)/(2\lambda_-)$, $b = -\epsilon/2$, $c = 1/2$, $d = -\epsilon a$, where $\epsilon \equiv \mathrm{sgn}(XV')$.

Using these eigenstates we can calculate the Berry connection vector, $\mathbf{A} \equiv -i\langle \psi^- | \nabla_\mathbf{k} | \psi^- \rangle$,

$$\mathbf{A} = \frac{1}{2}\nabla_\mathbf{k}\phi_\mathbf{k}, \quad \phi_\mathbf{k} = \tan^{-1}\left[\frac{Y}{X - \epsilon V'}\right]. \quad (13)$$

This implies for a line integral on a circular contour centered around any specific point on the nodal line,

$$\oint \mathbf{A} \cdot d\mathbf{k} = \frac{1}{2}[\phi_\mathbf{k}(\alpha = 2\pi) - \phi_\mathbf{k}(\alpha = 0)]. \quad (14)$$

The contour is in the plane perpendicular to the k_x direction and α is the azimuthal angle which defines a point of the contour. See Appendix B for a more detailed description. The function $\phi_\mathbf{k}(\alpha)$ has a singularity when the denominator of Eq. (13) vanishes. This happens on a 2D surface and intersects the k_y-k_z plane at the nodal line. Any such closed contour around the nodal line crosses this surface twice, with the value of $\phi_\mathbf{k}$ at each singularity contributing a value of π to the integral, so we obtain $\oint \mathbf{A} \cdot d\mathbf{k} = \pi$.

V. TOPOLOGICAL SUPERCONDUCTIVITY AND MAJORANA STATES

Having demonstrated that our model supports a Weyl nodal ring, we proceed by adding interactions in order to study the exotic superconducting states that emerge in the ground state of the interacting model.

We consider a mean-field Bogoliubov–de Gennes (BdG) Hamiltonian of the form

$$\hat{H}^{\mathrm{BdG}} = \frac{1}{2}\sum_\mathbf{k}(c_\mathbf{k}^\dagger c_{-\mathbf{k}})\hat{\mathcal{M}}(c_\mathbf{k} c_{-\mathbf{k}}^\dagger),$$

$$\hat{\mathcal{M}} \equiv \begin{pmatrix} \mathcal{H}_0(\mathbf{k}) - \mu & \Delta \\ \Delta^\dagger & -\mathcal{H}_0^\mathsf{T}(-\mathbf{k}) + \mu \end{pmatrix}. \quad (15)$$

The matrix $\mathcal{H}_0(\mathbf{k})$ corresponds to Eq. (1), and the gap function $\Delta = \mathbb{I}_{2\times2} \otimes i\Delta_0\sigma_y$, where $\mathbb{I}_{2\times2}$ is the 2×2 identity matrix and σ_y is a Pauli matrix.

We now solve the BdG equations in a slab geometry (with finite x dimension). The presence of interactions causes the nodal ring to split into two rings, which bound regions hosting different numbers of surface states with distinct topological characters (see the upper left panel of Fig. 4). These surface states are dispersionless even in the presence of a finite chemical potential (see the lower left panel of Fig. 4).

In order to characterize these surface states as Majorana states we examine the components of their wave functions. The Majorana states are defined by the property of their creation and annihilation operators, $\gamma_\mathbf{k}^\dagger = \gamma_{-\mathbf{k}}$. The Hamiltonian in Eq. (15), for the case of finite x dimension, is diagonalized by Bogoliubov operators,

$$\gamma_{k_\parallel}^\dagger = \sum_i a_{k_\parallel}^i c_{i,k_\parallel}^{\dagger(A)} + b_{k_\parallel}^i c_{i,k_\parallel}^{\dagger(B)} + c_{k_\parallel}^i c_{i,k_\parallel}^{\dagger(C)} + d_{k_\parallel}^i c_{i,k_\parallel}^{\dagger(D)}$$
$$+ e_{k_\parallel}^i c_{i,-k_\parallel}^{(A)} + f_{k_\parallel}^i c_{i,-k_\parallel}^{(B)} + g_{k_\parallel}^i c_{i,-k_\parallel}^{(C)} + h_{k_\parallel}^i c_{i,-k_\parallel}^{(D)}, \quad (16)$$

where i labels the layer in the finite direction, and $k_\parallel = (k_y, k_z)$. The Majorana condition $\gamma_\mathbf{k}^\dagger = \gamma_{-\mathbf{k}}$ implies (up to an arbitrary phase),

$$a_{k_\parallel}^i = (e_{-k_\parallel}^i)^*, \quad b_{k_\parallel}^i = (f_{-k_\parallel}^i)^*,$$
$$c_{k_\parallel}^i = (g_{-k_\parallel}^i)^*, \quad d_{k_\parallel}^i = (h_{-k_\parallel}^i)^*. \quad (17)$$

In the right column of Fig. 4 we plot the amplitudes $c_{k_\parallel}^i$, and $g_{-k_\parallel}^i$ of the wave function for a Majorana surface state (top) at $k_y/2\pi = k_z/2\pi = 0.05$ and a drumhead state (bottom) at $k_y/2\pi = k_z/2\pi = 0.228$. Both states are localized on the edge of the system, however, only the Majorana state satisfies the condition of Eq. (17). We plot only the amplitudes $c_{k_\parallel}^i$ and $g_{-k_\parallel}^i$, but we note that all components of the Majorana state satisfy Eq. (17).

VI. SUMMARY AND CONCLUSIONS

Since its introduction, the SSH model has been one of the most important and well-studied models of condensed matter physics. The model has served as a foundational description of many of the novel concepts that have since become central to the field of condensed matter. In this paper we have introduced an analytically soluble 3D extension of the SSH model which, for appropriate choices of its hopping

parameters, describes well the band structure of crystalline polyacetylene as obtained by DFT. We observe that when a specific diagonal hopping is made sufficiently large a Weyl nodal ring forms in the band structure, whose projection bounds drumhead topological surface states. This intriguing state of 3D stacked SSH chains, in principle, can be realized by applying high pressure on the crystallized polyacetylene or by doping or intercalation of atoms which can increase the effective 3D hopping amplitudes. We find that both the $P2_1/a$ and the $P2_1/n$ structures, either of which may be stabilized under pressure, support a nodal-ring state, and that this state is stable across a large parameter regime, which offers a broad window for experimental realizations. Starting from this Weyl nodal-ring structure, by adding an interaction coupling electrons on carbon atoms of different sublattices within the same unit cell, we find topological superconductivity supporting both Bogoliubov-Weyl quasiparticles and annular Majorana surface states. In addition to the fascinating physics this system displays, it also provides a different perspective on a well-known model, placing it again at the heart of modern condensed matter physics and reorienting it towards the recent direction of exotic topological phenomena, including topological superconductivity.

ACKNOWLEDGMENTS

APPENDIX A: TB MODEL FOR $P2_1/n$ STRUCTURE

In Fig. 5 we provide the unit cell for our TB model of the $P2_1/n$ structure of crystalline polyacetylene. This model yields four bands of the form

$$E_1^{\pm}(\mathbf{k}) = -2t_y \cos(k_y a_y) - 2t_z \cos(k_z a_z)$$
$$\pm \sqrt{X^2 + Y^2 + V^2 + 2|V||X|},$$
$$E_2^{\pm}(\mathbf{k}) = -2t_y \cos(k_y a_y) - 2t_z \cos(k_z a_z)$$
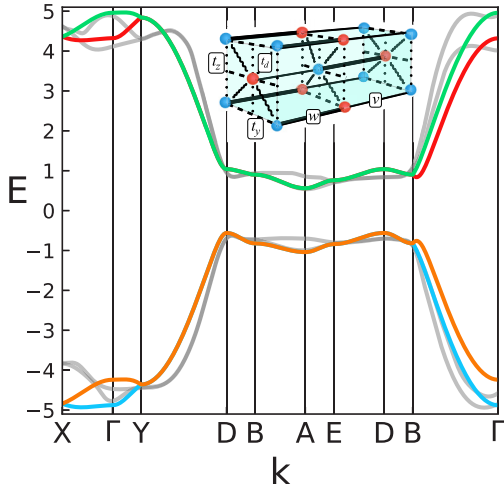$$\pm \sqrt{X^2 + Y^2 + V^2 - 2|V||X|}, \qquad (A1)$$

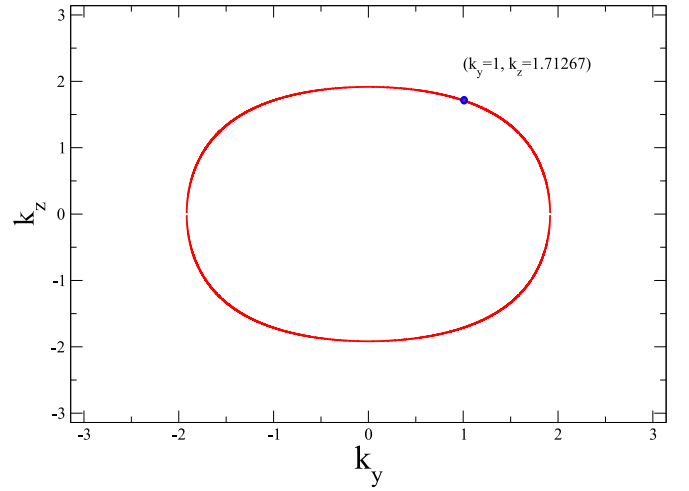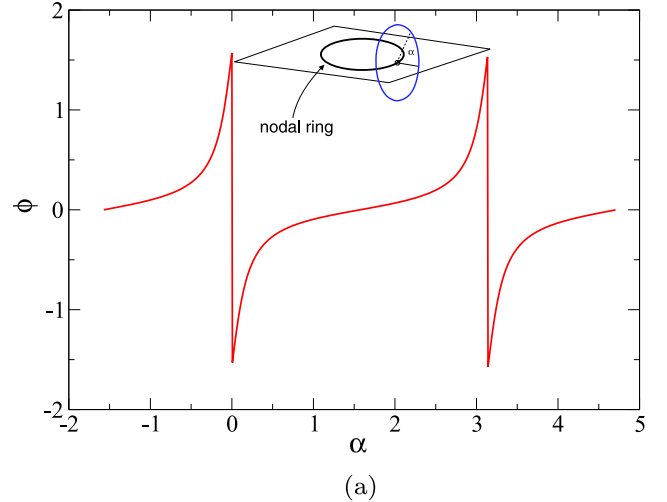FIG. 5. Unit cell and band structure for the model of $P2_1/n$ crystalline polyacetylene.
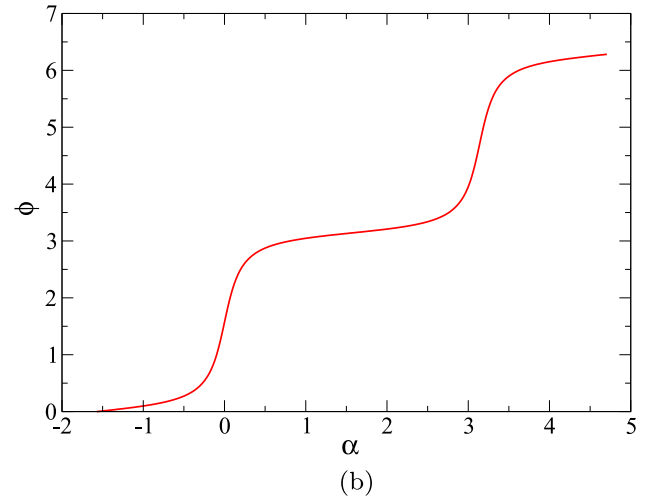

FIG. 6. An example of the nodal ring.

(a)

(b)

FIG. 7. (a) The function ϕ is plotted as a function of the angle α, by taking its value in the interval $(-\pi/2, \pi/2]$. (b) The function ϕ is plotted as a function of the angle α by choosing the value, from the multitude of its values, that yields a continuous function.

which are plotted along with the DFT results (gray curves).

APPENDIX B: NODAL LINE AND BERRY PHASE CALCULATION

Figure 6 demonstrates an example of a nodal line on the k_y-k_z plane, which is obtained for a definite value of the ratio parameter r defined by Eq. (12) of the main text. The blue circle in the figure denotes a particular point on the nodal line, with coordinates $(k_y, k_z) = (1, 1.712\,67)$, that we have selected to demonstrate below how the integral in Eq. (14) of the main text is evaluated.

After selecting a point on the nodal line, which lies on the k_y-k_z plane, we define a circular loop around the nodal line which lies on a plane perpendicular to the nodal line. This loop is schematically drawn in Fig. 7 as an inset. Then, we wish to calculate the line integral $\oint \mathbf{A} \cdot d\mathbf{k}$ around this loop. The instantaneous position on the loop is specified by the angle α shown in the inset of Fig. 7.

In Fig. 7 the function $\phi_{\mathbf{k}}(\alpha)$ is plotted as a function of α as extracted from Eq. (13) numerically. However, we note that the function $\tan^{-1}$ is a multivalued function and the function plotted in Fig. 7(a) only gives the value of the function in the interval $[-\pi/2, \pi/2]$. This definition only works correctly when the angle is needed in an interval of α which contains no singularity or branch cut. However, the function $\tan\phi_{\mathbf{k}}$ has a singularity when the denominator of Eq. (13) vanishes. This happens on a 2D surface which is perpendicular to the k_x direction and intersects the k_y-k_z plane at the nodal line. So, the path crosses this surface twice. Since we are looking for a smooth, i.e., continuous, transition of the phase ϕ as a function of α we need to pick the value (from the multitude of its possible values) of $\tan^{-1}$ that yields a continuous line. This implies that we need to add π for each of the singularities shown in Fig. 7(a). Namely, we need to choose the solution which is plotted in Fig. 7(b). Therefore, we obtain

$$\oint \mathbf{A} \cdot d\mathbf{k} = \frac{1}{2}[\phi_{\mathbf{k}}(\alpha = 2\pi) - \phi_{\mathbf{k}}(\alpha = 0)] = \pi. \quad \text{(B1)}$$

[1] W. P. Su, J. R. Schrieffer, and A. J. Heeger, Phys. Rev. Lett. **42**, 1698 (1979).

[2] A. J. Heeger, S. Kivelson, J. R. Schrieffer, and W. P. Su, Rev. Mod. Phys. **60**, 781 (1988).

[3] M. J. Rice and E. J. Mele, Phys. Rev. Lett. **49**, 1455 (1982).

[4] J. Zak, Phys. Rev. Lett. **62**, 2747 (1989).

[5] M. Z. Hasan and C. L. Kane, Rev. Mod. Phys. **82**, 3045 (2010).

[6] N. P. Armitage, E. J. Mele, and A. Vishwanath, Rev. Mod. Phys. **90**, 015001 (2018).

[7] Z. K. Liu, B. Zhou, Y. Zhang, Z. J. Wang, H. M. Weng, D. Prabhakaran, S.-K. Mo, Z. X. Shen, Z. Fang, X. Dai, Z. Hussain, and Y. L. Chen, Science **343**, 864 (2014).

[8] L. Lu, Z. Wang, D. Ye, L. Ran, L. Fu, J. D. Joannopoulos, and M. Soljačić, Science **349**, 622 (2015).

[9] B. Q. Lv, H. M. Weng, B. B. Fu, X. P. Wang, H. Miao, J. Ma, P. Richard, X. C. Huang, L. X. Zhao, G. F. Chen, Z. Fang, X. Dai, T. Qian, and H. Ding, Phys. Rev. X **5**, 031013 (2015).

[10] S.-Y. Xu, I. Belopolski, N. Alidoust, M. Neupane, G. Bian, C. Zhang, R. Sankar, G. Chang, Z. Yuan, C.-C. Lee, S.-M. Huang, H. Zheng, J. Ma, D. S. Sanchez, B. Wang, A. Bansil, F. Chou, P. P. Shibayev, H. Lin, S. Jia *et al.*, Science **349**, 613 (2015).

[11] L. Huang, T. M. McCormick, M. Ochi, Z. Zhao, M.-T. Suzuki, R. Arita, Y. Wu, D. Mou, H. Cao, J. Yan, N. Trivedi, and A. Kaminski, Nat. Mater. **15**, 1155 (2016).

[12] J. Jiang, Y. Liu, Z. K.and Sun, H. F. Yang, C. R. Rajamathi, Y. P. Qi, L. X. Yang, C. Chen, H. Peng, C.-C. Hwang, S. Z. Sun, S.-K. Mo, I. Vobornik, J. Fujii, S. S. P. Parkin, C. Felser, B. H. Yan, and Y. L. Chen, Nat. Commun. **8**, 13973 (2017).

[13] A. A. Burkov, M. D. Hook, and L. Balents, Phys. Rev. B **84**, 235126 (2011).

[14] Y. Kim, B. J. Wieder, C. L. Kane, and A. M. Rappe, Phys. Rev. Lett. **115**, 036806 (2015).

[15] Y. Chen, Y. Xie, S. A. Yang, H. Pan, F. Zhang, M. L. Cohen, and S. Zhang, Nano Lett. **15**, 6974 (2015).

[16] C. Fang, H. Weng, X. Dai, and Z. Fang, Chin. Phys. B **25**, 117106 (2016).

[17] R. Yu, H. Weng, Z. Fang, X. Dai, and X. Hu, Phys. Rev. Lett. **115**, 036807 (2015).

[18] G. Bian, T.-R. Chang, H. Zheng, S. Velury, S.-Y. Xu, T. Neupert, C.-K. Chiu, S.-M. Huang, D. S. Sanchez, I. Belopolski, N. Alidoust, P.-J. Chen, G. Chang, A. Bansil, H.-T. Jeng, H. Lin, and M. Z. Hasan, Phys. Rev. B **93**, 121113(R) (2016).

[19] G. Bian, T.-R. Chang, R. Sankar, S.-Y. Xu, H. Zheng, T. Neupert, C.-K. Chiu, S.-M. Huang, G. Chang, I. Belopolski, D. S. Sanchez, M. Neupane, N. Alidoust, C. Liu, B. Wang, C.-C. Lee, H.-T. Jeng, C. Zhang, Z. Yuan, S. Jia *et al.*, Nat. Commun. **7**, 10556 (2016).

[20] M. Atala, M. Aidelsburger, J. T. Barreiro, D. Abanin, T. Kitagawa, E. Demler, and I. Bloch, Nat. Phys. **9**, 795 (2013).

[21] N. R. Cooper, J. Dalibard, and I. B. Spielman, Rev. Mod. Phys. **91**, 015005 (2019).

[22] Z.-Y. Wang, X.-C. Cheng, B.-Z. Wang, J.-Y. Zhang, Y.-H. Lu, C.-R. Yi, S. Niu, Y. Deng, X.-J. Liu, S. Chen, and J.-W. Pan, Science **372**, 271 (2021).

[23] B. Song, C. He, S. Niu, L. Zhang, Z. Ren, X.-J. Liu, and G.-B. Jo, Nat. Phys. **15**, 911 (2019).

[24] T. Meng and L. Balents, Phys. Rev. B **86**, 054504 (2012).

[25] G. Y. Cho, J. H. Bardarson, Y.-M. Lu, and J. E. Moore, Phys. Rev. B **86**, 214514 (2012).

[26] G. Bednik, A. A. Zyuzin, and A. A. Burkov, Phys. Rev. B **92**, 035153 (2015).

[27] Y. Li and F. D. M. Haldane, Phys. Rev. Lett. **120**, 067003 (2018).

[28] S. Kobayashi and M. Sato, Phys. Rev. Lett. **115**, 187001 (2015).

[29] M. Alidoust, K. Halterman, and A. A. Zyuzin, Phys. Rev. B **95**, 155124 (2017).

[30] P. Rosenberg, N. Aryal, and E. Manousakis, Phys. Rev. B **100**, 104522 (2019).

[31] R. Nandkishore, Phys. Rev. B **93**, 020506(R) (2016).

[32] Y. Wang and R. M. Nandkishore, Phys. Rev. B **95**, 060506(R) (2017).

[33] P.-H. Fu, J.-F. Liu, and J. Wu, Phys. Rev. B **102**, 075430 (2020).

[34] Z. Faraei and S. A. Jafari, Phys. Rev. B **100**, 035447 (2019).

[35] P. Vogl and D. K. Campbell, Phys. Rev. B **41**, 12797 (1990).

[36] Y.-H. Chan, C.-K. Chiu, M. Y. Chou, and A. P. Schnyder, Phys. Rev. B **93**, 205132 (2016).